DETECTION OF FEMUR FRACTURES IN X-RAY IMAGES

TIAN TAI PENG

NATIONAL UNIVERSITY OF SINGAPORE
2002

Name : Tian Tai Peng
Degree : Master of Science
Dept : Computer Science
Thesis Title : Detection of Femur Fractures in X-Ray Images

Abstract

Many people suffer from hip fractures, especially people suffering from osteoporosis. Doctors rely on radiographs, i.e., x-ray images, to establish the precise nature of a fracture. An automated fracture detection system can assist the doctor by performing the first examination to screen out the easier cases, leaving a small number of difficult cases and the second confirmation to the doctors. This thesis outlines a fracture detection system and focus on measuring the neck-shaft angle of the femur. The accuracy of using the neck-shaft angle for determining femur fractures is also tested.

Keywords:

Neck-shaft angle, femur fractures, active contour

DETECTION OF FEMUR FRACTURES IN X-RAY IMAGES

Tian Tai Peng
(B. Sc. (Hon.) in Computer and Information Sciences, NUS)

A THESIS SUBMITTED
FOR THE DEGREE OF MASTER OF SCIENCE
DEPARTMENT OF COMPUTER SCIENCE
SCHOOL OF COMPUTING
NATIONAL UNIVERSITY OF SINGAPORE
2002

Contents

List of Figures

List of Tables

List of Algorithms

Summary

Many people suffer from hip fractures, especially people suffering from osteoporosis. Doctors rely on radiographs, i.e., x-ray images, to establish the precise nature of a fracture. An automated fracture detection system can assist the doctor by performing the first examination to screen out the easier cases, leaving a small number of difficult cases and the second confirmation to the doctors.

This thesis outlines a fracture detection system, and focuses on the extraction of the femur bone contour and measurement of the femoral neck-shaft angle. Snakes combine with Gradient Vector Flow field are used to extract the femur outline. Given the boundary contour, the orientations of the femoral shaft and the femoral neck are computed. The angle between these two orientations is the neck-shaft angle. Using the neck-shaft angle as a criterion for discriminating between fractured and healthy femurs, the method achieves a correct classification rate of 94.5%.

Chapter 1

Introduction

1.1 Motivation

Many people suffer from fractures of the bone, especially people suffering from osteoporosis. Osteoporosis is a disease characterized by low bone mass and deterioration of bone tissue (Fig 1.1). This condition leads to increased bone fragility and risk of fracture. If not prevent or left untreated, the disease can progress painlessly until a bone breaks. Osteoporosis related bone fractures occur typically in the hip, spine and wrist (Fig 1.2). Any bone can be affected but of special concern are fractures of the hip as such fractures almost always requires hospitalization and major surgery. It can also impair a person's ability to walk unassisted and may cause prolonged or permanent disability.

Some 800 people suffer hip fractures in Singapore every year due to osteoporosis and Singapore General Hospital (SGH) sees about 350 of such

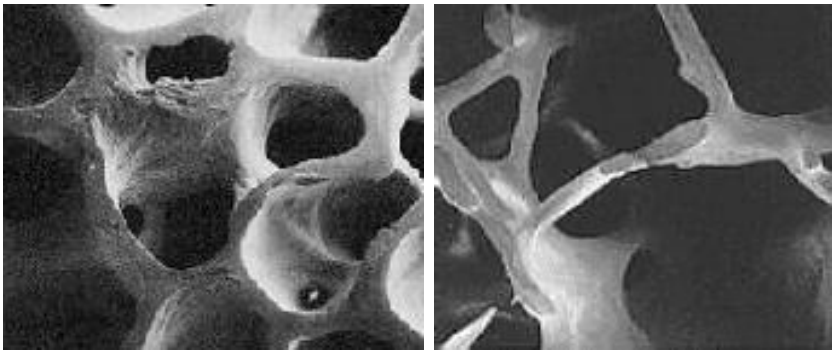

(a) Healthy Bone (b) Osteoporotic Bone

Figure 1.1: Comparison between osteoporotic and healthy bone.

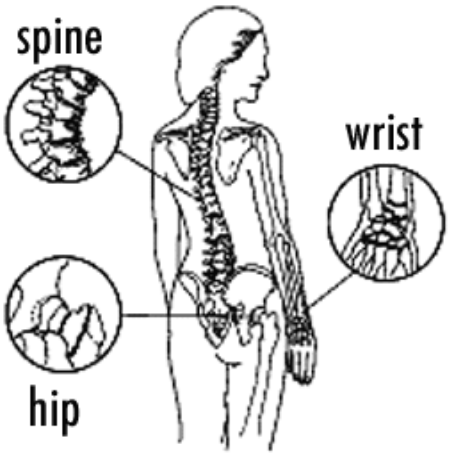

Figure 1.2: Common fracture sites for osteoporosis

patients each year. According to studies, a quarter of the hip fractured patients die within the first year and seventy percent of the survivors require walking aids, became wheelchair bound or bedridden [33].

Doctors rely on radiographs, i.e., x-ray images, to establish the precise nature of a fracture (see Fig 1.3). Currently doctors in Singapore General Hospital examine each radiograph twice to determine whether a fracture exists. Manual inspection of radiographs for fractures is both a tedious and time consuming process. On top of that, doctors will get too tired to perform the task reliably after examining numerous radiographs. As some fractures are easier to identify than others, an automated fracture detection system can assist the doctor by performing the first examination to screen out the easier cases, leaving a small number of difficult cases and the second confirmation to the doctors. Automatic interpretation of medical images can relieve some of the labor intensive work of the doctors thus improving the accuracy of the diagnosis.

In this research, emphasis will be placed on detecting common hip fractures of the femur as such fractures account for the largest portion of fracture incidents in the population. Section 1.2 will explain in detail the anatomy of the femur and Section 1.3 will describe different fractures of the femur.

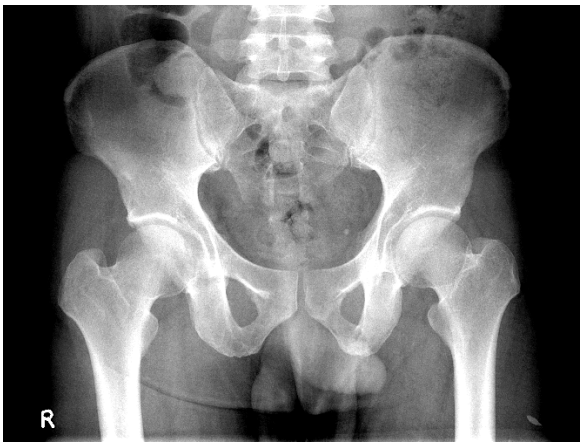

Figure 1.3: A radiograph example of the hip.

1.2 The Femur

The femur is the longest and strongest bone in the skeleton. It is connected to the pelvis to form the hip joint and connected to the tibia to form the upper knee joint (Fig. 1.4). Each femur directly bears the weight of the upper body.

The femur is almost perfectly cylindrical in the greater part of its extent. It is divisible into a body and two extremities: the upper and lower extremities.

The Body or Shaft

The body or shaft, almost cylindrical in form, is a little broader above than in the center (Fig 1.5). It is slightly arched, so as to be convex in

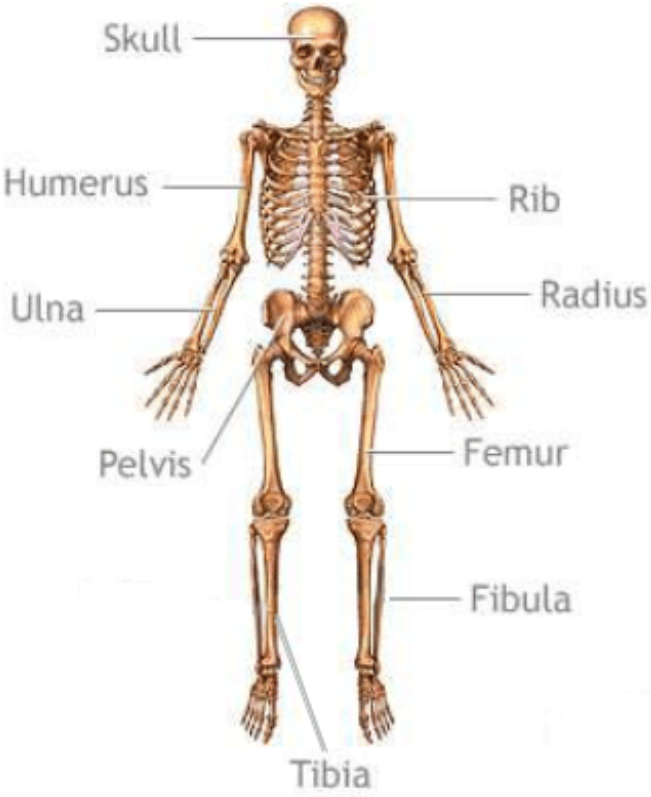

Figure 1.4: Anterior skeleton anatomy

front and concave behind.

Upper Extremity

The upper extremity comprises the head, neck, a greater trochanter and a lesser trochanter (Fig. 1.5). The head is globular and the neck is a flattened pyramidal bone connecting the head with the shaft of the femur. The neck forms an angle of about 125 degrees with the shaft, but it varies in inverse proportion to the development of the pelvis. The angle also varies considerably in different persons of the same age. The greater and lesser trochanters provide leverage to the muscles that rotate the thighs on it axes.

Lower Extremity

The lower extremity is somewhat cuboid in form and it consists of two oblong eminences known as the condyle (Fig 1.6)

Neck-Shaft Angle

The neck-shaft angle is commonly used by doctors to detect fractures in the femur. The neck-shaft angle is determined by measuring the angle subtended by the lines drawn through the axes of the femoral shaft and the femoral neck (Fig 1.7). The neck-shaft angle for a healthy adult femur is approximately 120 to 130 degrees.

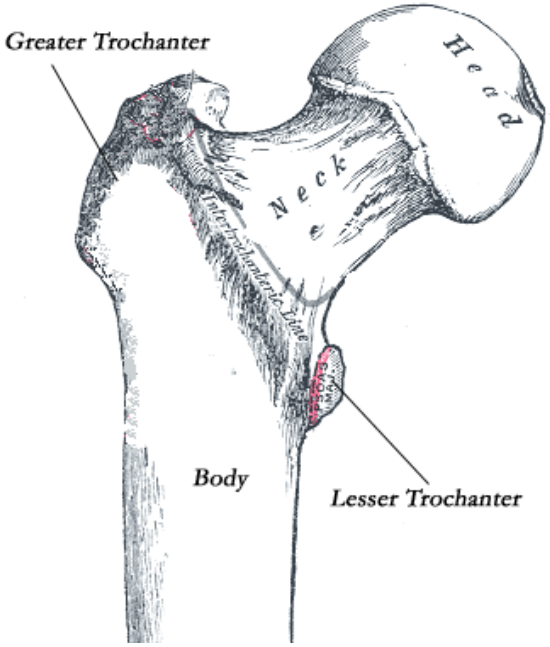

Figure 1.5: Upper extremity and body of the femur.

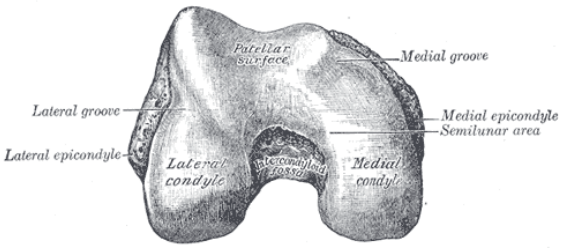

Figure 1.6: Lower extremity of the femur.

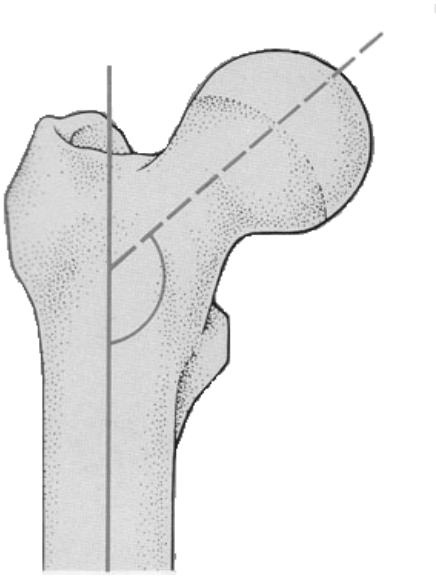

Figure 1.7: Neck-shaft angle

1.3 Anatomy of Fracture

A fracture may be a complete break in the continuity of a bone or it may be an incomplete break or crack. The fracture site is often used to classify the type fracture. Hip fractures can be classified as head, neck, intertrochanteric, trochanteric or subtrochanteric. The following is a classification found in [16].

Femoral Neck Fractures

Femoral neck fractures occur between the end of the femoral head and the intertrochanteric region (Fig 1.8).

Intertrochanteric Fractures

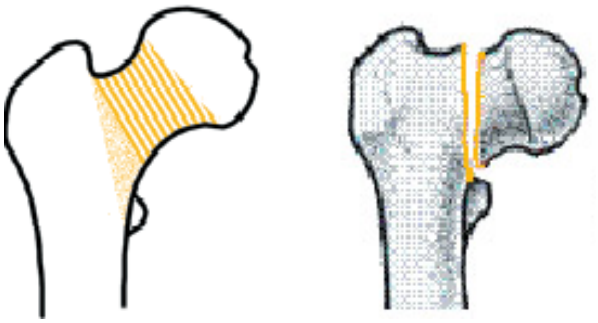

(a) (b)

Figure 1.8: Femoral neck fracture (b) occurs at the femoral neck region (a).

Intertrochanteric fractures occur in the bone between the femoral neck and the femoral shaft (Fig 1.9). These fractures may involve both the greater and lesser trochanter.

Greater Trochanteric Fractures

This type of fracture occurs in the greater trochanter (Fig 1.10). It may occur in elderly patients suffering from osteoporosis and may result from direct trauma such as a fall.

Subtrochanteric Fractures

Subtrochanteric fractures occur between the lesser trochanter and the shaft of the femur (Fig 1.11).

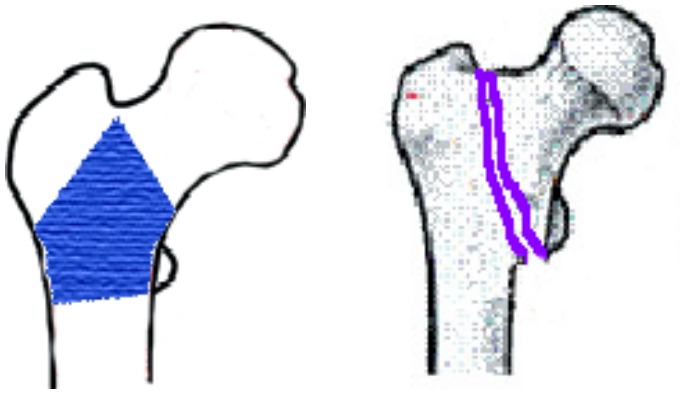

(a) (b)

Figure 1.9: Intertrochanteric fracture (b) occurs at the intertrochanteric region (a).

(a) (b)

Figure 1.10: Greater trochanteric fracture (b) occurs at the greater trochanteric region (a).

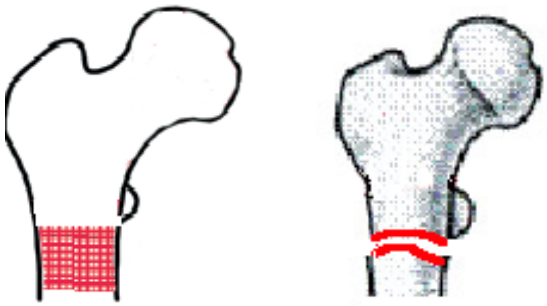

(a) (b)

Figure 1.11: Subtrochanteric fracture (b) occurs at the subtrochanteric region (a).

1.4 Project Objectives

The overall goal of the project is to develop a system to detect fractures of the femur automatically, which consists of three modules (Figure 1.12).

Firstly, given an x-ray image of the hip, the Femur Localization module will need to find the location of the left and right femur in the image. Precise object localization is a difficult problem in computer vision. This module is investigated by another student and is thus not the focus of this thesis.

Next, to analyze the geometry of the femur, a more accurate outline of the femur is needed. The locations of the two femurs identified by the "Femur Localization" module will serve as the initial search locations in the "Femur Contour Extraction module". Active contours, also know as snakes [23] are used in the "Femur Contour Extraction" module. If a snake is placed close

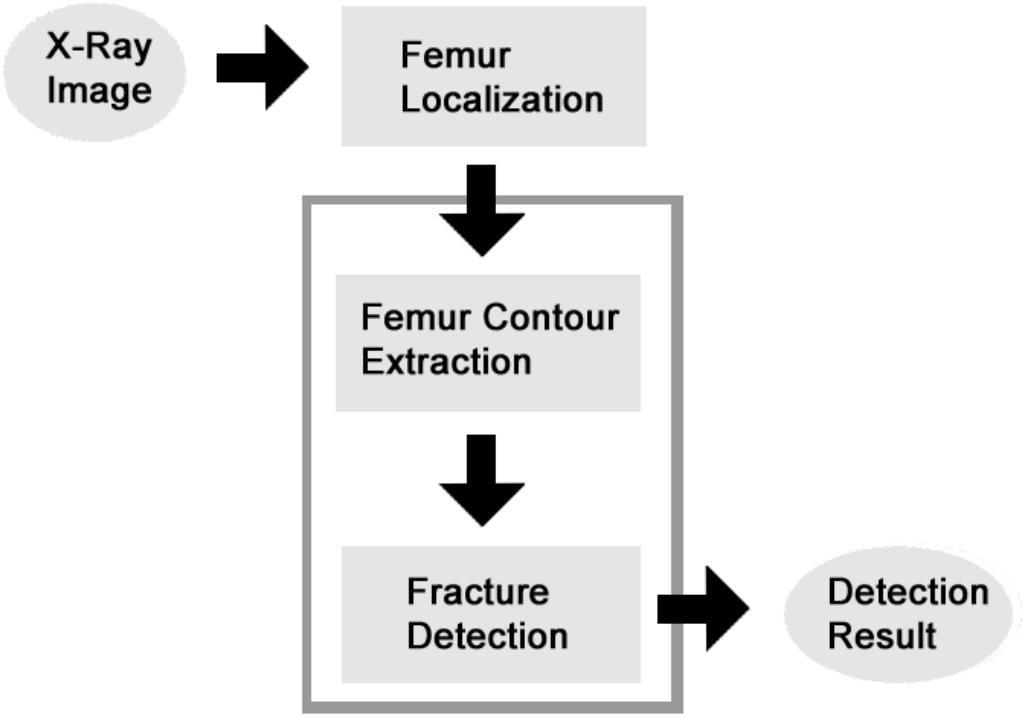

Figure 1.12: Project Overview.

to the femur outline, the snake algorithm will make use of image features to guide and deform itself to converge on the outline of the femur. The output from the snake algorithm is a more accurate description of the femur's boundary contour and is more suitable for analyzing potential fracture of the femur.

Finally, in the "Fracture Detection" module, the contour of the femurs will be analyzed to compute the neck-shaft angles. Any femurs with abnormal neck-shaft angles will be classified as fractured.

In summary, the main objective of this thesis is to develop the algorithms necessary for the "Femur Contour Extraction" and "Fracture Detection" modules.

1.5 Organization of Thesis

After highlighting the motivation and project objectives in this chapter, related work will be reviewed in Chapter 2. The details of the algorithms for the "Femur Contour Extraction" and "Fracture Detection" module will be discussed in Chapter 3 and Chapter 4 respectively. Experimental results of the algorithms are discussed in Chapter 5. Finally, future direction for this work is highlighted in Chapter 6, followed by the conclusion in Chapter 7.

Chapter 2

Related Work

Medical image interpretation is a hard problem as any non-trivial algorithm will involve some form of automated system to understand the information contained in the image. Fortunately, the general shape, location and orientation of the objects of interest are usually known in medical image analysis. Such information may be represented in a model of the object as initial conditions, constraints on model parameters or constraints during model fitting procedure. Once the model has been established, analysis of the model can take place.

There is a wealth of model representations used in medical image interpretation literature. They include free-form deformable models [23, 31, 32], parametric deformable templates [36], point distribution model [11, 12], graphical templates [3] and skeleton-based templates [29, 30].

2.1 Free-Form Deformable Model

Free-form deformable models contains no global structure except for some regularization constraints such as continuity or smoothness constraint of the boundary. Without any constraints on the global shape, it can represent arbitrary shape as long as it satisfies the regularization constraints.

Active contours [23, 31, 32] or snakes are good examples of free-form deformable models. These contours will evolve under the influence of image forces (such a edges or intensity) that pull it towards desired features and internal forces that enforce smoothness and continuity constraints on the contour.

This approach of evolving based on local image features makes the snake more vulnerable to image noise and initial position. Many improvements have been suggested to overcome these shortcomings [1, 9, 10, 34].

With an initialization that places the snake close to the object boundaries, the snake algorithm can extract an accurate representation of the object's outline. Such detailed outlines are useful for constructing higher level representation of the contour such as centroid-radii model [8, 20] and the curvature primal sketch [4, 26].

2.1.1 Centroid-Radii Model

The centroid-radii model [8, 20] samples a set of points from the outline of the object. These points will be used to re-parameterize the original contour in terms of the distance from the centroid to the points (call radii lines) as well as the angle from a reference line to the radii lines.

This approach is useful for objects with fairly consistent shape but in the case of femur fractures, the centroid may be drastically different from one case to the other.

2.1.2 Curvature Primal Sketch

Curvature primal sketch [4] extracts significant changes in curvature along the contour across varying levels of details (i.e., multiple level of curve smoothing) called the generalized scale space image of planar curve [26]. These changes are classified into five different groups of primitives based on the curvature discontinuity and are used for matching purposes.

This technique has been successfully used for object recognition [27] but the representation is too sparse for fracture detection. For example in some fracture incidents, it may not increase or decrease the number of curvature primal sketch primitives. Hence, this will pose a problem when trying to detect fractures based on such primitives. Furthermore, the lesser trochanter

may not be present in all the femur images and may thus flag off a wrong alert during fracture detection.

2.2 Parametric Deformable Templates

Deformable templates [36] are hand-crafted models represented by a collection of parameterized curves. These curves are uniquely described by a set of parameters. Changing the parameters will change the geometric shape of the template.

A good example is the work of Yuille et al. [36] who constructed deformable templates to extract facial features. Their parametric models for eye and mouth templates consist of circles and parabolic curves. The shape of the template is controlled by the radius of the circle and the parameters of the parabola. A set of regularizing constraints are used to impose on the shape to limit the deformations such that it result in reasonable shapes. By defining energy terms describing the deformation of the template and energy terms for the image features, the detection algorithm will become a minimization procedure based on the energy terms.

For this technique a good initialization of the contour is necessary for good results. On top of that, this scheme is not suitable for shapes with complicated outlines as it will be difficult to describe the outline using a small set

of curves. Secondly the approximate orientation, scale and translation of the object to be segmented has to be known beforehand to craft the regularizing constraints and it will be difficult to build a template encompassing all the different classes of fractures.

2.3 Point Distribution Model

The Point Distribution Models (PDM) [14, 25] approach assumes the existence of a set of training examples from which to derive a statistical description of the shape and its variation. This approach is most useful for describing objects that have well understood general shape but which cannot be easily described by a rigid model.

The shape is defined as all the geometrical information that remains when location, scale and rotational effects are filtered out from an object [15]. One way to represent a shape is to locate a finite number of points on the boundary of the object (a sequence of pixel co-ordinates) called landmark points. To ensure that the set of points satisfy the definition of a shape, the effects of scale, translation and rotation are filtered out by aligning the training samples. A common procedure for aligning the data is the Procrustes Analysis [6, 13, 18]. Principal Component Analysis space is used to extract a parameterized model of the training data and with this parameterized model,

it allows new shapes, different from the training samples, to be synthesized.

Point distribution models are used in Active Shape Models [11, 12, 13] to search for objects of interest in an image using the PDM. The search is formulated as an optimization problem in which the difference between the synthesized shape and the actual image is to be minimized. This algorithm has been proven to be successful in medical segmentation [5] and analysis [19].

The main drawback of this approach is that the PDM requires human intervention to annotate landmark points in the training images and this can be very time consuming. Currently automatic and semi-automatic methods are being developed to aid this task of annotating landmark points.

2.4 Graphical Template Model

The model in a Graphical Template [2, 3] is represented as a graph. Vertices will represent landmark points and edges represent important geometric relations among the landmark points. Such graphs are usually hand-crafted and differ from application to application.

The Graphical Template Model is used mainly as a registration algorithm. The algorithm attempts to localize the model by scanning for candidates of each of the landmarks. These landmarks are extracted from the image using robust local operators. The collection of landmark points which satisfy the

graph constraints and yielding the best match, will be chosen to represent the object in the image.

2.5 Skeleton Based Model

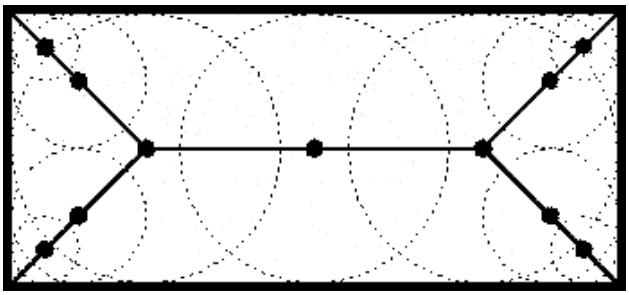

Figure 2.1: The medial axis (solid line) is defined in terms of maximal discs (dotted circles).

A medial axis, or skeleton, of a shape is defined as the locus of the centers of all maximal discs contained in the shape. A maximal disc contained in the shape is any circle with that touches the boundary of the shape at two or more points (Figure 2.1).

An intuitive way to construct the medial axis is the prairie fire transform. Imagine that the interior of the object is composed of dry grass and a fire is started at all points of the boundary. The fire will move in at uniform speed towards the middle of the object. At points where two fronts of fire meet, they will extinguish each other. The locations where the fronts meet are the

locations of the medial axis points.

Shape modeling typically requires a robust variant of the traditional medial axis so that small changes in the outline of the shape does not severely alter its topology [17]. Most skeleton extraction algorithms require a segmented image as the input. An exception is the algorithm proposed by Pizer et al. [30] where they introduced a model comprising of nets of medial and boundary primitives. This model can estimate the boundary of the object and its medial axis based on the intensity gradient in the original gray scale image.

Chapter 3

Extraction of Femur Contour

An overview of the algorithm for extracting the contour of the femur is shown in Figure 3.1. It consists of a sequence of processes. First a modified Canny edge detector (Section 3.1) is used to compute the edges from the input x-ray image of the hip followed by computing the Gradient Vector Flow field [34] (Section 3.3) for the edges. Next, the snake algorithm [23] (Section 3.2) combine with the Gradient Vector Flow will move the active contour, i.e, the snake to the contour of the femur.

For the snake algorithm to work well, the initial points of the snake should be placed close to the femur boundary. Currently the initial points of the snake are placed manually as automatic placement of the initial points of the snake is a difficult problem and it is not the focus of this thesis.

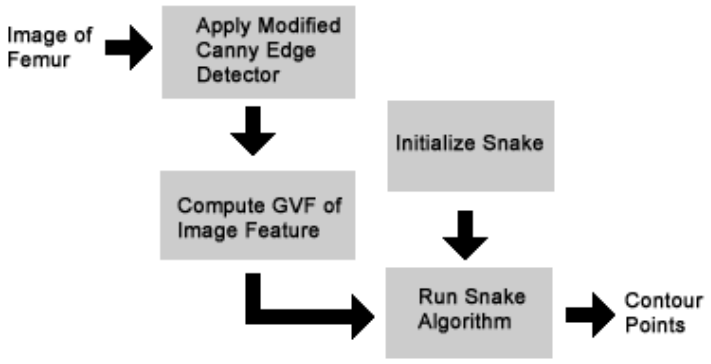

Figure 3.1: Femur contour extraction algorithm.

3.1 Modified Canny Edge Detection

The Canny edge detector [7] takes as input a gray scale image and produces as output an image showing the position of the edges. It works as follows. The image is first smoothed by Gaussian convolution. Next, a simple 2D first derivative operator is applied to the smoothed image to highlight regions of the image with high first derivatives. Using the gradient direction calculated, the algorithm performs non-maxima suppression to eliminate pixels whose gradient magnitude is lower than its two neighbors along the gradient direction. Finally these thin edges are linked up using a technique involving double thresholding. Although Canny edge detector works well in detecting the outline of the femur, it also detects a large number of spurious edges close to the shaft (Figure 3.2b). Such spurious edges will affect the snake's

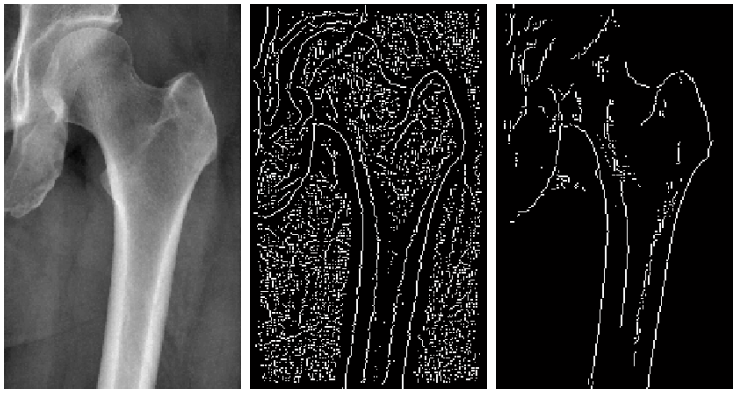

(a) (b) (c)

Figure 3.2: Result of Canny edge detection. (a) Original femur image. (b) Canny edge with low threshold values. (c) Canny edge with more smoothing and higher threshold values. Notice that a large portion of femoral head has disappeared (c).

convergence on the outline of the femur and have to be removed. Attempting to remove the spurious edges by increasing the smoothing effect will reduce these spurious edges but the edge information at the femur head will also be lost (Figure 3.2c). Contributing to the problem is the fact that the femur head overlaps with the hip bones and edge magnitudes of the femur head in this region is low. Hence simple thresholding based on edge magnitude will fail .

The problem of preserving femur head edges and at the same time removing spurious edges can be solved by incorporating information from the intensity image into the Canny edge algorithm. Looking at the original intensity x-ray image of the femur (Figure 3.2a), areas containing bones have higher intensity than non-bone regions. Hence this information can be used to distinguish spurious edges from femur head edges. The Canny edge detector with a small smoothing effect is used to detect the femur head edges while spurious edges with both low intensity value and low gradient magnitude values are removed (Figure 3.3d).

In summary, a pixel is marked as an non-edge point if

1. it is detected by Canny edge detector,

2. it has an intensity lower than a threshold Γ, and

3. it has an edge magnitude lower than the same threshold Γ.

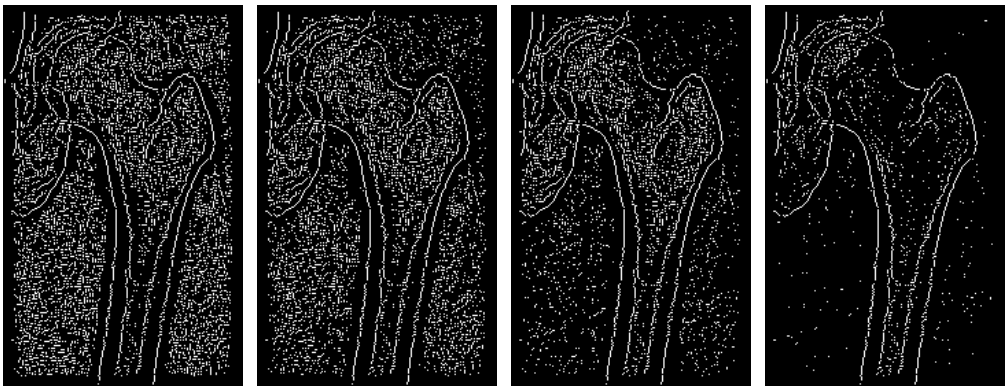

(a) (b) (c) (d)

Figure 3.3: Modified Canny edge detection with various threshold values. (a) 20%, (b) 50%, (c) 70%, (d) 90%

The threshold Γ is actually a percentage value. In the current implementation, a non-edge pixel must have an intensity and an edge magnitude lower than 90% of the total pixels. Figure 3.3 shows the edge detection results with various threshold values.

3.2 Snakes and Active Contours

Snakes or active contours became popular after the seminal paper by Kass, Witkin and Terzopoulos [23]. The contour extraction module makes use of snake to snap onto the contour of the femur (Figure 3.4).

Snakes are formulated as energy-minimizing contours controlled by two

forces:

1. Internal contour forces which enforce the smoothness constraint.

2. Image forces which attracts the contour to the desired features, in this case, edges.

$$\mathbf{E}_{snake} = \int_0^1 \mathbf{E}_{int}(\mathbf{v}(s)) + \mathbf{E}_{image}(\mathbf{v}(s))ds \tag{3.1}$$

Representing the position of the snake parametrically by $\mathbf{v}(s) = (x(s), y(s))$, the energy of a snake $\mathbf{E}_{snake}$ (Eqn 3.1) is a sum of the internal energy $\mathbf{E}_{int}$ of the snake and the image energy $\mathbf{E}_{image}$.

Internal Energy

The internal energy $\mathbf{E}_{int}$ is composed of a first-order term controlled by $\alpha(s)$ and a second order term controlled by $\beta(s)$.

$$\mathbf{E}_{int} = \left(\alpha(s)\left|\mathbf{v}_s(s)\right|^2 + \beta(s)\left|\mathbf{v}_{ss}(s)\right|^2\right)/2 \tag{3.2}$$

The terms $\mathbf{v}_s$ and $\mathbf{v}_{ss}$ represents the first and second derivative of $\mathbf{v}$ respectively. $\alpha(s)$ characterizes the tension along the snake and $\beta(s)$ characterizes the bending of the curve. Currently, $\alpha(s)$ and $\beta(s)$ are set as values α and β.

Image Energy

In the current implementation, the snake is programmed to converge onto edges and modified Canny edge detector (Section 3.1) is used to compute the edges $\mathbf{E}_{edge}$ from the input images. The image energy $\mathbf{E}_{image}$ will be $\mathbf{E}_{edge}$ weighted appropriately by a negative weight $-w_{edge}$.

$$\mathbf{E}_{image} = -w_{edge}\mathbf{E}_{edge} \tag{3.3}$$

Minimization Procedure

A snake that minimize the energy functional $\mathbf{E}_{snake}$ must satisfy the following Euler equations [23] :

$$\alpha x_{ss} + \beta x_{ssss} + \frac{\partial \mathbf{E}_{image}}{\partial x} = 0 \tag{3.4}$$

$$\alpha y_{ss} + \beta y_{ssss} + \frac{\partial \mathbf{E}_{image}}{\partial y} = 0 \tag{3.5}$$

Where x_{ss} and x_{ssss} are the second and fourth derivatives of x, similarly for y_{ss} and y_{ssss}.

In computer implementation, Eqn 3.1 is discretized as follows :

$$\mathbf{E}_{snake} = \sum_{i=1}^{n} \mathbf{E}_{int}(i) + \mathbf{E}_{image}(i) \tag{3.6}$$

Using a vector notation with $\mathbf{v}_i = (x_i, y_i) = (x(ih), y(ih))$ and approximating the derivatives x_{ss}, x_{ssss}, y_{ss} and y_{ssss} in Eqn 3.4 and 3.5 using

finite difference, $\mathbf{E}_{int}(i)$ can be expanded as :

$$\mathbf{E}_{int}(i) = \frac{\alpha_i \left|\mathbf{v}_i - \mathbf{v}_{i-1}\right|^2}{2h^2} + \frac{\beta_i \left|\mathbf{v}_{i-1} - 2\mathbf{v}_i + \mathbf{v}_{i+1}\right|^2}{2h^4} \tag{3.7}$$

For a closed contour snake, we can define $\mathbf{v}(0) = \mathbf{v}(n)$. Define $f_x(i) = \partial\mathbf{E}_{image}/\partial x_i$ and $f_y(i) = \partial\mathbf{E}_{image}/\partial y_i$ where the derivatives are approximated by finite difference. Therefore the corresponding Euler equations (Eqn 3.4, 3.5) become

$$\begin{aligned}&\alpha_i(\mathbf{v}_i - \mathbf{v}_{i-1}) - \alpha_{i+1}(\mathbf{v}_{i+1} - \mathbf{v}_i) + \beta_{i-1}(\mathbf{v}_{i-2} - 2\mathbf{v}_{i-1} + \mathbf{v}_i)\\ &- 2\beta_i(\mathbf{v}_{i-1} - 2\mathbf{v}_i + \mathbf{v}_{i+1}) + \beta_{i+1}(\mathbf{v}_i - 2\mathbf{v}_{i+1} + \mathbf{v}_{i+2}) + (f_x(i), f_y(i)) = 0\end{aligned} \tag{3.8}$$

Rewriting the above Euler equations in matrix form we have

$$\mathbf{A}\mathbf{x} + \mathbf{f}_x(\mathbf{x}, \mathbf{y}) = 0 \tag{3.9}$$

$$\mathbf{A}\mathbf{y} + \mathbf{f}_y(\mathbf{x}, \mathbf{y}) = 0 \tag{3.10}$$

Where $\mathbf{A}$ is a penta-diagonal banded matrix and below is an example for a 7 point closed contour with constant α and β :

$$\mathbf{A} = \begin{pmatrix} c_1 & d_1 & e_1 & 0 & 0 & a_1 & b_1 \\ b_2 & c_2 & d_2 & e_2 & 0 & 0 & a_2 \\ a_3 & b_3 & c_3 & d_3 & e_3 & 0 & 0 \\ 0 & a_4 & b_4 & c_4 & d_4 & e_4 & 0 \\ 0 & 0 & a_5 & b_5 & c_5 & d_5 & e_5 \\ e_6 & 0 & 0 & a_6 & b_6 & c_6 & d_6 \\ d_7 & e_7 & 0 & 0 & a_7 & b_7 & c_7 \end{pmatrix} \quad \begin{aligned} a_i &= \beta_{i-1} \\ b_i &= -\alpha_i - 2\beta_{i-1} - 2\beta_i \\ c_i &= \alpha_i + \alpha_{i+1} + \beta_{i-1} + 4\beta_i + \beta_{i+1} \\ d_i &= -\alpha_{i+1} - 2\beta_i - 2\beta_{i+1} \\ e_i &= \beta_{i+1} \end{aligned} \tag{3.11}$$

To solve Eqn 3.9, the snake is made dynamic by treating $\mathbf{x}$ and $\mathbf{y}$ as

function of time and solved iteratively [23].

$$\mathbf{x}(t+1) = (\mathbf{A} + \gamma\mathbf{I})^{-1}(\gamma\mathbf{x}(t) - \mathbf{f}_x(\mathbf{x}(t), \mathbf{y}(t))) \tag{3.12}$$

$$\mathbf{y}(t+1) = (\mathbf{A} + \gamma\mathbf{I})^{-1}(\gamma\mathbf{y}(t) - \mathbf{f}_x(\mathbf{x}(t), \mathbf{y}(t))) \tag{3.13}$$

where γ is the Euler step size. $(\mathbf{A} + \gamma\mathbf{I})^{-1}$ can be calculated by LU decomposition in $O(n)$ time, where n is the length of the snake.

3.3 Gradient Vector Flow

Gradient Vector Flow (GVF) [34] is a type of external force for active contours. The GVF was created to overcome two shortcomings of the original active contour formulation i.e poor convergence to concave boundaries and sensitivity to initialization. GVF is computed as a diffusion of the gradient vectors of a gray-level edge map derived from the image.

The GVF field is defined as the vector field $\mathbf{G}(x, y) = (\mathbf{q}(x, y), \mathbf{r}(x, y))$ that minimizes the energy functional

$$\varepsilon = \int\int \mu(\mathbf{q}_x^2 + \mathbf{q}_y^2 + \mathbf{r}_x^2 + \mathbf{r}_y^2) + |\nabla\mathbf{E}|^2 \, |\mathbf{G} - \nabla\mathbf{E}|^2 \, dxdy \tag{3.14}$$

where $\mathbf{E}$ is an edge map $E(x, y)$ derived from the image. Using calculus of variations, the GVF can be found by solving the following Euler equations

$$\mu\nabla^2\mathbf{q} - (\mathbf{q} - \mathbf{E}_x^2 + \mathbf{E}_y^2) = 0 \tag{3.15}$$

$$\mu\nabla^2\mathbf{r} - (\mathbf{r} - \mathbf{E}_y^2 + \mathbf{E}_y^2) = 0 \tag{3.16}$$

Equations 3.15 and 3.16 can be solved by treating $\mathbf{q}$ and $\mathbf{r}$ as functions of time and solving

$$\begin{aligned}\mathbf{q}(x,y,t+1) =& \mu\nabla^2\mathbf{q}(x,y,t) \\ &- (\mathbf{q}(x,y,t) - \mathbf{E}_x(x,y)) \cdot (\mathbf{E}_x(x,y)^2 + \mathbf{E}_y(x,y)^2)\end{aligned} \tag{3.17}$$

$$\begin{aligned}\mathbf{r}(x,y,t+1) =& \mu\nabla^2\mathbf{r}(x,y,t) \\ &- (\mathbf{r}(x,y,t) - \mathbf{E}_y(x,y)) \cdot (\mathbf{E}_x(x,y)^2 + \mathbf{E}_y(x,y)^2)\end{aligned} \tag{3.18}$$

The steady state solution (as $t \to \infty$) of equations 3.17 and 3.18 is the require solution of the Euler equations 3.15 and 3.16. Details of the numerical implementation for Eqn 3.15 and 3.16 can be found in [35].

3.4 Combining Snake with GVF

The snake algorithm is combine with the external force computed by the GVF to improve the performance of snake. To incorporate the GVF into the snake algorithm, after computing the solution $\mathbf{q}$ and $\mathbf{r}$ in equation 3.17 and 3.18, replace $\mathbf{f}_x$ and $\mathbf{f}_y$ from equation 3.12 and 3.13 with $\mathbf{q}$ and $\mathbf{r}$ respectively.

With the GVF snake, only a small number of initialization points are needed to start the snake algorithm (Figure 3.4) and successive iterations

of the algorithm will re-distribute the snake points more regularly along the contours.

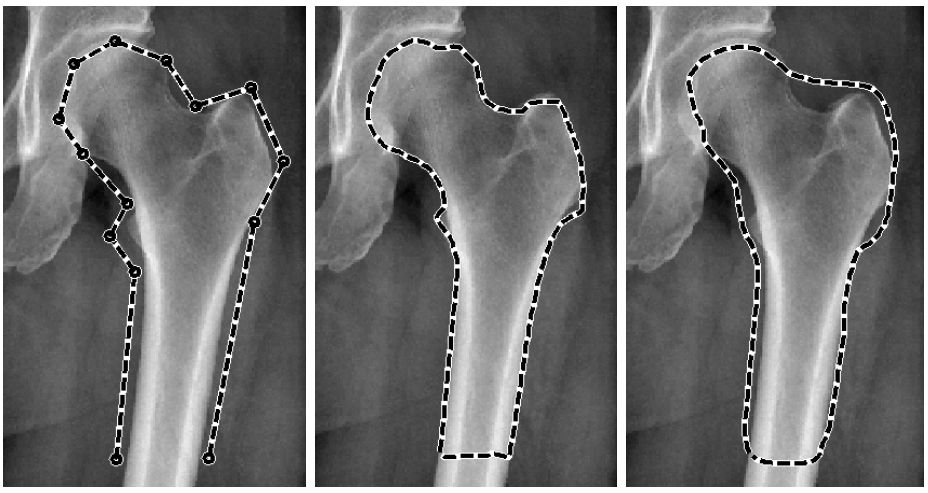

(a) (b) (c)

Figure 3.4: With small number of initialization points in (a) an accurate outline of the femur can be obtained using snake combine with GVF (b). (c) shows the result of using snake without GVF and it is difficult to get the snake to snap onto the concave structure at the femoral neck.

Chapter 4

Measuring Neck-Shaft Angle from Femur Contour

The contour lines along the femoral shaft are almost parallel. If normal lines are drawn from one side of the shaft to the opposite side and compute the midpoints of these lines, then the mid-points would be aligned parallel to the shaft (Figure 4.1). We call these normal lines *level lines* as each line denotes a level along the femoral shaft. Section 4.1 will explain in detail how such lines are constructed and Section 4.2 will how the midpoints of the level lines are used to determine the orientation of the shaft. The level lines are also useful for computing the orientation of the femoral neck, which is elaborated in Section 4.3. Once the shaft orientation and the neck orientation have been computed, the neck-shaft angle can be easily computed as the angle the neck

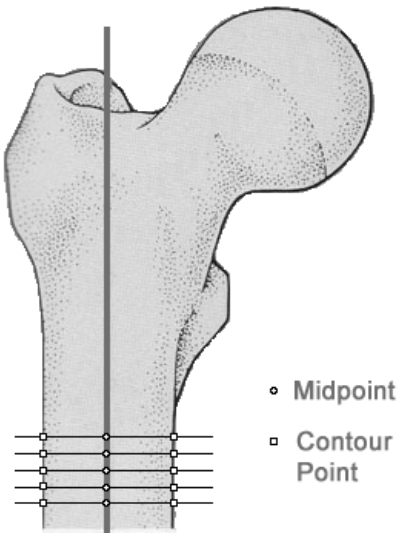

Figure 4.1: Normal lines on the femur shaft.

and shaft orientation.

4.1 Computing Level Lines

The construction of the level lines depends on the normals of the contour points and there are a few ways to compute the normal for a point on the contour. A common approach is to use finite difference to estimate the derivative and hence derive the normal direction. This technique uses a small number of points in the neighborhood of the point of interest to derive the normal. It is sensitive to small changes in the neighbors' positions of the points.

On the other hand, with a dense sampling of points along the contour, a larger set of points can be used to compute the normal at a point using Principal Component Analysis (PCA) [21, 22]. To compute the normal of a contour point, choose a neighborhood of points around the point of interest. This set of points represents a segment of the contour and PCA is applied to this segment of points. Given a set of points in 2D, PCA returns two eigenvectors and their associated eigenvalues. The eigenvector with the largest eigenvalue will point in the direction parallel to this segment of points and the other eigenvector gives the normal direction at the point of interest.

Once the normal for each point on the contour has been calculated, the set of level lines $\mathbf{L}$ can be computed. Let $\mathbf{p}_i$ and $\mathbf{p}_j$ denote the vector representation of two points on the contour and $\mathbf{n}_i$ and $\mathbf{n}_j$ be the associated unit normals. Then the line $l(\mathbf{p}_i, \mathbf{p}_j)$ that connects points $\mathbf{p}_i$ and $\mathbf{p}_j$ is a level line if

$$|\mathbf{n}_i \cdot \mathbf{n}_j| \approx |(\mathbf{p}_i - \mathbf{p}_j) \cdot \mathbf{n}_i| \approx |(\mathbf{p}_i - \mathbf{p}_j) \cdot \mathbf{n}_j| \approx 1 \tag{4.1}$$

In the current implementation, two orientations $\mathbf{v}_1$ and $\mathbf{v}_2$ are similar i.e., $|\mathbf{v}_1 \cdot \mathbf{v}_2| \approx 1$ if $|\mathbf{v}_1 \cdot \mathbf{v}_2| \geq 0.98$

4.2 Computing Orientation of the Femoral Shaft

The orientation of the femur shaft can be computed by extracting the midpoints of the level lines on the shaft (Figure 4.2). Given level lines $l_i(\mathbf{p}_i^1, \mathbf{p}_i^2)$ and the midpoints $\mathbf{m}_i = \frac{1}{2}(\mathbf{p}_i^1 + \mathbf{p}_i^2)$, sort $\mathbf{m}_i$ in decreasing order of y-coordinates of $\mathbf{m}_i$ (assuming the origin is at the top-left corner of the image) and call them $\mathbf{m}'_i$. The first midpoint $\mathbf{m}'_1$ must be a midpoint along the femoral shaft. Now for each midpoint $\mathbf{m}'_i$, $i \geq 2$, include $\mathbf{m}'_i$ as a shaft point if $\mathbf{m}'_i$ is near to $\mathbf{m}'_{i-1}$.

After finding the midpoints of the shaft, the PCA algorithm is used to estimate the orientation of the midpoints. The eigenvector with the largest eigenvalue computed from the PCA algorithm will represent the orientation of the shaft midpoints.

4.3 Computing the Orientation of the Femoral Neck

The computation of femoral neck's orientation is more complicated because there is no obvious axis of symmetry. The algorithm consist of three main steps.

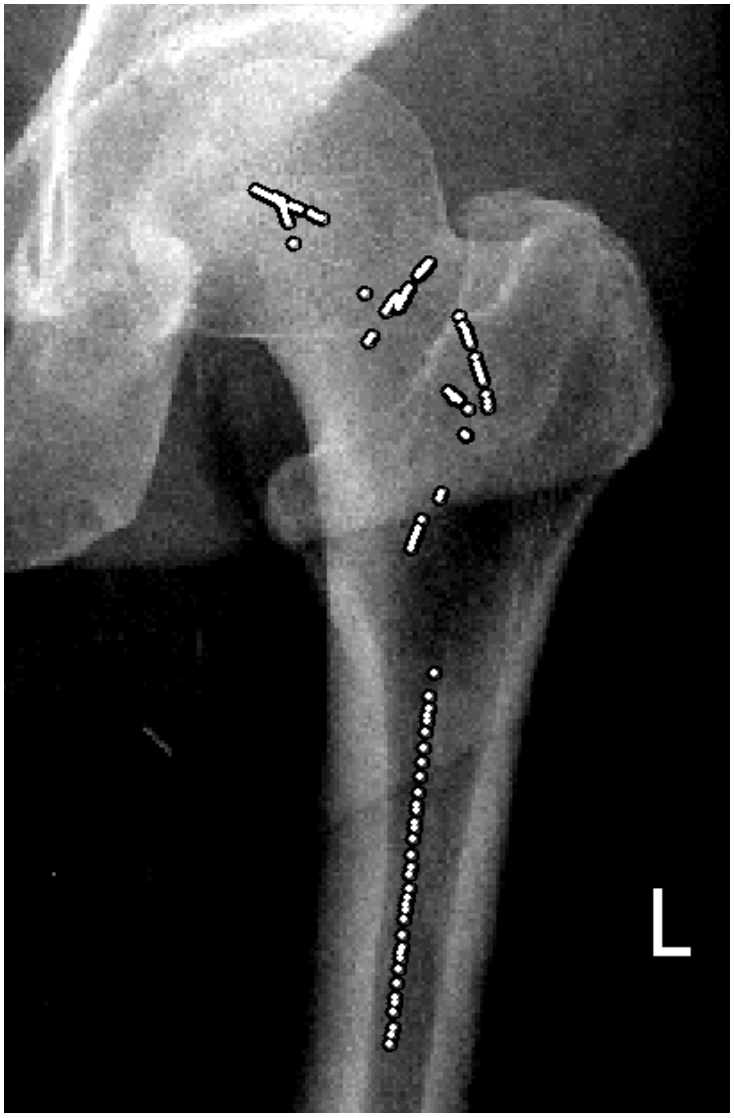

Figure 4.2: The midpoints of the level lines are shown as white dots. The midpoints along the shaft give a good estimate of the orientation of the femoral shaft.

1. compute an initial estimate of the neck orientation (Section 4.3.1) ,
2. smooth the femur contour (Section 4.3.2), and
3. search for the best axis of symmetry using the initial neck orientation estimate (Section 4.3.3).

4.3.1 Computing Initial Estimation of Femoral Neck's Orientation

The longest level lines in the upper region of the femur always cut through the contour of the femoral head (Figure 4.3). Given this observation, an adaptive clustering algorithm [24] is used to cluster long level lines at the femoral head into bundles of closely spaced level lines with similar orientations. The bundle with the largest number of lines is chosen, and the average orientation of the level lines in this bundle is regarded as the initial estimate of the orientation of the femoral neck.

The adaptive clustering algorithm is useful as it does not need to choose the number of clusters before hand. The general idea is to group the level lines such that in each group, the level lines are similar in terms of orientation and spatial position. The adaptive clustering algorithm groups a level line into its nearest cluster if the orientation and midpoint of the cluster is close. If a level line is far enough from any of the existing clusters, a new cluster

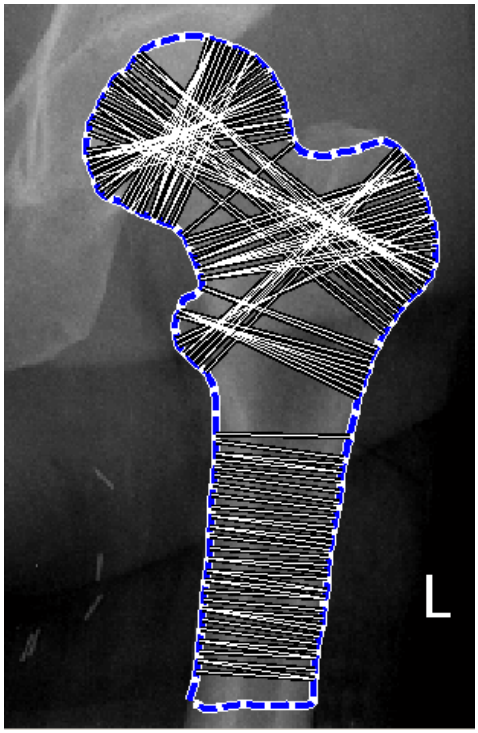

Figure 4.3: Level lines along the femoral neck intersects the femoral head contour.

will be created for this level line. For level lines that are neither close nor far enough, they will be left alone and not assigned to any cluster.

With the adaptive clustering algorithm, it ensures each cluster has a minimum similarity of R_1 for the cluster orientation and minimum similarity of R_2 for the mid-points distance. The algorithm also ensures that the cluster differs by a similarity of at most S_1 and S_2 for the orientation and mid-points distance respectively. Varying the values of R_1, R_2, S_1 and S_2 controls the

granularity of clustering and the amount of overlapping between clusters.

Algorithm 1: Computing initial estimation of femoral neck's orientation.

Input: Set of level lines $\mathbf{L} = \{\mathbf{l}_i\}$, with corresponding orientation $\mathbf{u}_i$ and midpoint $\mathbf{m}_i$.

Output: A point $\mathbf{p}_{head}$ on the femoral head contour.

Note that each cluster k is characterized by an orientation $\mathbf{u}_k$ and a midpoint $\mathbf{m}_k$.

1 **foreach** $l_i \in \mathbf{L}$ **do**
Find cluster k such that orientation $\mathbf{u}_k$ is most similar to $\mathbf{u}_i$ and $\mathbf{m}_k$ is close to $\mathbf{m}_i$.
If $|\mathbf{u}_k \cdot \mathbf{u}_i| \geq R_1$ and $|\mathbf{m}_i - \mathbf{m}_k| \leq R_2$ (i.e similar in orientation and spatially close).
Then include l_i in cluster k
Else if $|\mathbf{u}_k \cdot \mathbf{u}_i| \leq S_1$ and $|\mathbf{m}_i - \mathbf{m}_k| \geq S_2$
Then create a new cluster with line l_i.
end

2 Update cluster orientation and midpoint
Repeat 1 and 2 until convergence

4.3.2 Smoothing the Original Contour

Consider a parametric equation for a curve $\mathbf{v} = (x(s), y(s))$ and $g(s, \sigma)$ is a 1-D Gaussian kernel of width σ then $X(s, \sigma)$ and $Y(s, \sigma)$ represents the components of a smoothed curve,

$$X(s, \sigma) = x(s) * g(s, \sigma) \tag{4.2}$$

$$Y(s, \sigma) = y(s) * g(s, \sigma) \tag{4.3}$$

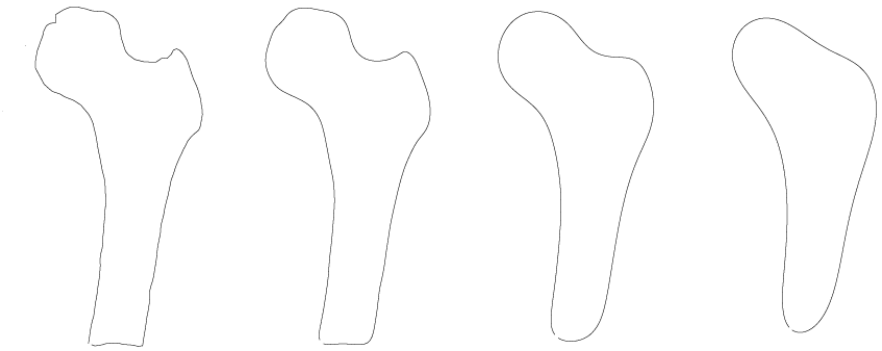

(a) Original (b) $\sigma = 2$ (c) $\sigma = 6$ (d) $\sigma = 10$

Figure 4.4: Contour smoothing. (a) Original femur contour. (b,c,d) smooth contours with different σ.

Observe that in Figure 4.4(c) the outline of the femoral head and neck is almost symmetrical after sufficient smoothing has been applied to the curve. The algorithm exploits this symmetry to estimate the orientation of the neck. Currently σ is chosen to be 5.

4.3.3 Computing the Axis of Symmetry for the Femoral Head and Neck

The general idea of determining the axis of symmetry is to find a line through the femoral neck and head such that the contour of the head and neck coincides with its own reflection about the line (Figure 4.6).

4.3.3 Computing the Axis of Symmetry for the Femoral Head and Neck

Given a point $\mathbf{p}_k$ along the contour of the femoral head and neck, obtain the midpoint $\mathbf{m}_i$ along the line joining contour point $\mathbf{p}_{k-i}$ and $\mathbf{p}_{k+i}$. That is, we obtain a midpoint for each pair of contour points on the opposite sides of $\mathbf{p}_k$ (Figure 4.5(a)). Now, we can fit a line l_k through the midpoints $\mathbf{m}_i$ to obtain a candidate axis of symmetry (Figure 4.5b). If the contour is perfectly symmetrical, and the correct axis of symmetry is obtained, then each contour point $\mathbf{p}_{k-i}$ is exactly the mirror reflection of $\mathbf{p}_{k+i}$. So the error E_k for l_k is

$$E_k = \frac{1}{n} \sum_{i=-n/2}^{n/2} \left| \mathbf{p}_{k+i} - \mathbf{p}'_{k-i} \right| \tag{4.4}$$

where $\mathbf{p}'_{k-i}$ is the reflection of $\mathbf{p}_{k-i}$ about l_k. E_k indicates how good is l_k as an axis of symmetry. The best fitting axis of symmetry is a midpoint fitting line l_t associated with $\mathbf{p}_t$ that minimizes the error:

$$E_t = \min_k E_k \tag{4.5}$$

4.3.3 Computing the Axis of Symmetry for the Femoral Head and Neck

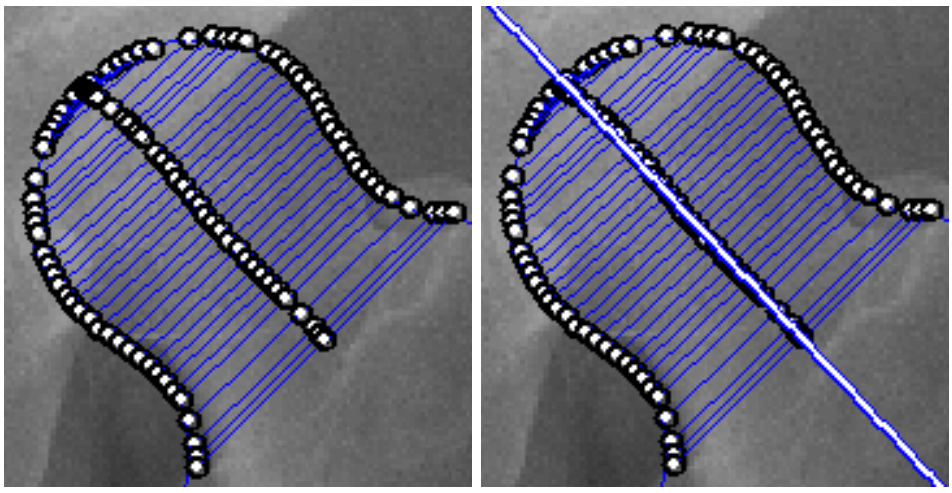

(a) (b)

Figure 4.5: Generating a candidate axis of symmetry. Outline of the contour and midpoints of the pairing (a). Fitting a line l_k through the midpoints (b).

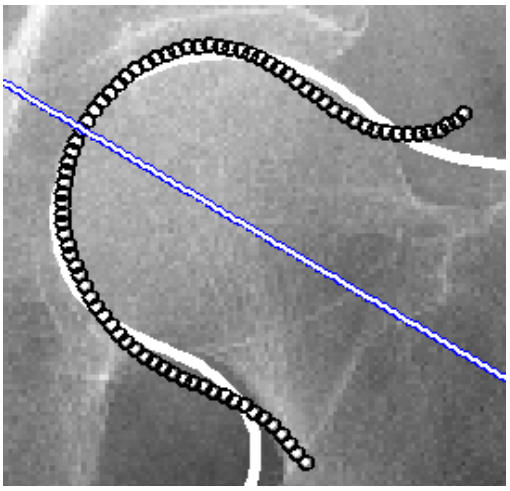

Figure 4.6: Determining axis of symmetry of femoral neck. The white contour denotes the smoothed contour of the femoral head and neck, and black circles are the reflection of the contour points about the straight line.

Chapter 5

Test Results and Discussion

Manual measurement of neck-shaft angles turns out to be quite inconsistent. So, there is no accurate and consistent ground truth for assessing the accuracy of the algorithm that measures the neck-shaft angle. Instead, experiments are conducted to determine how accurate can the measured neck-shaft angle be used to distinguish healthy femurs from fractured femur.

5.1 Classification using Neck-Shaft Angle

5.1.1 Test Setup

A set of 64 radiographic images of the hip were obtained. Of these 64 hip images, 19 of them contained fractures. Out of the 19 hip fractures, 12 were left femur fractures and 7 were right femur fractures. Each image contains

at most one fracture.

Three measurements were taken for each radiographic image: the neck-shaft angles for the left and right femur and the absolute difference between the left and right neck-shaft angles. The doctors frequently compare the left and right femur to look for significant differences between them. Hence, another classification will be based on the difference of the left and right neck-shaft angles.

5.1.2 Test Results

A summary of the result of running neck-shaft angle measurement of the left and right femurs can be found in Figure 5.1 and Figure 5.2 respectively. The summary for the difference of left and right neck-shaft angles is shown in Figure 5.3. The x-axis represents the different test cases and the y-axis represents the neck-shaft angle measured in degrees. The dots represent the healthy femurs and the box around a dot denotes that the femur is fractured.

From Figure 5.1 and Figure 5.2, we can see that setting a threshold at 116 degrees yields the best classification accuracy. For the left-right difference, Figure 5.3 shows that a threshold of 11 degrees yields the best classification accuracy.

A summary of the classification results can be found in Table 5.1. The sec-

5.1.2 Test Results

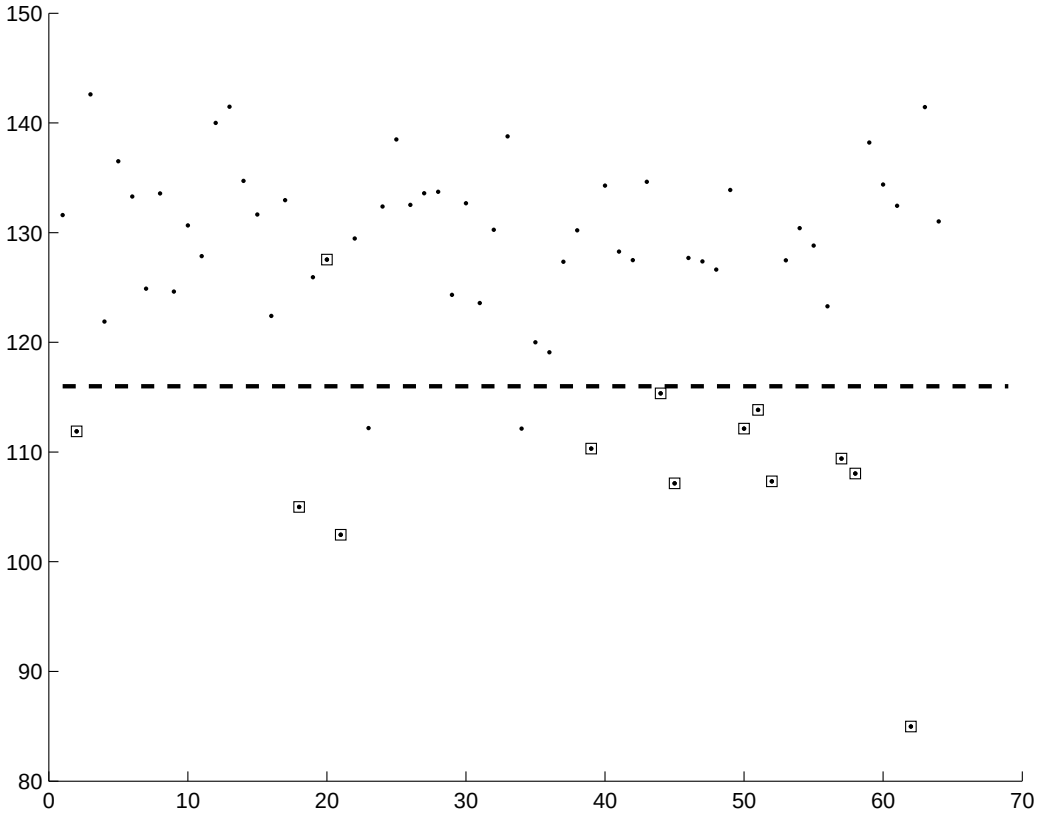

Figure 5.1: Neck-shaft angle measurement for left femurs. The dotted line denotes the classification threshold.

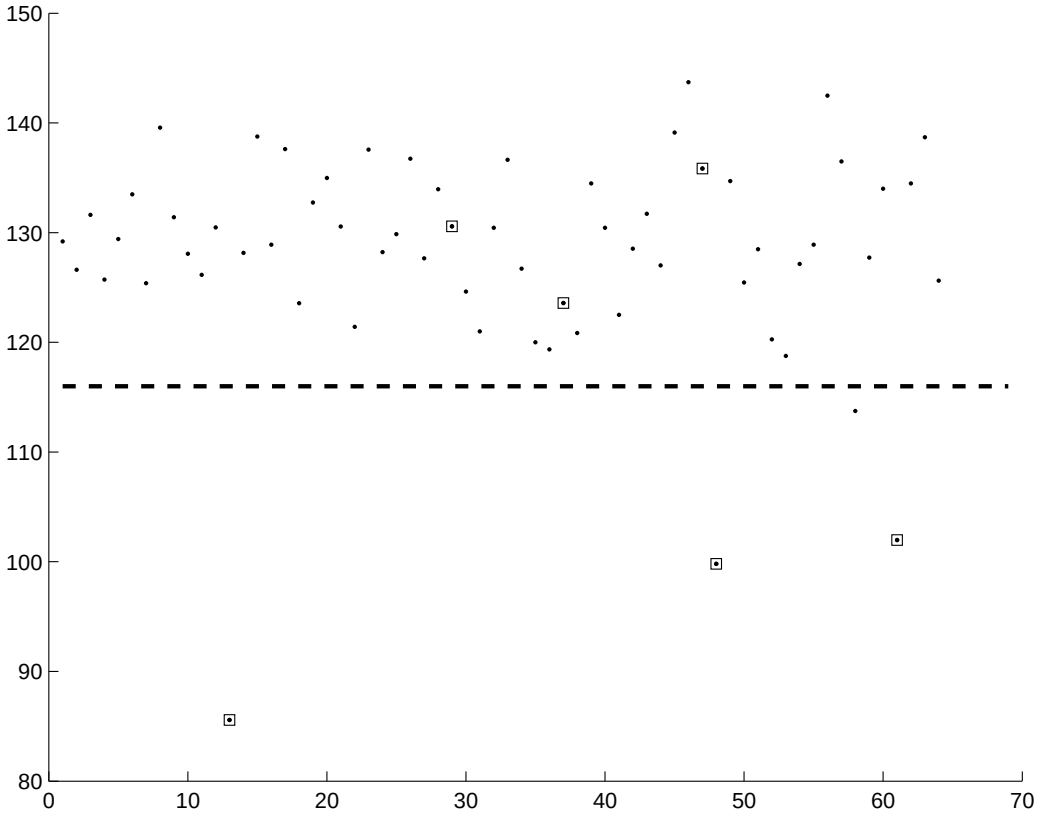

Figure 5.2: Neck-shaft angle measurement for right femurs.The dotted line denotes the classification threshold.

5.1.2 Test Results

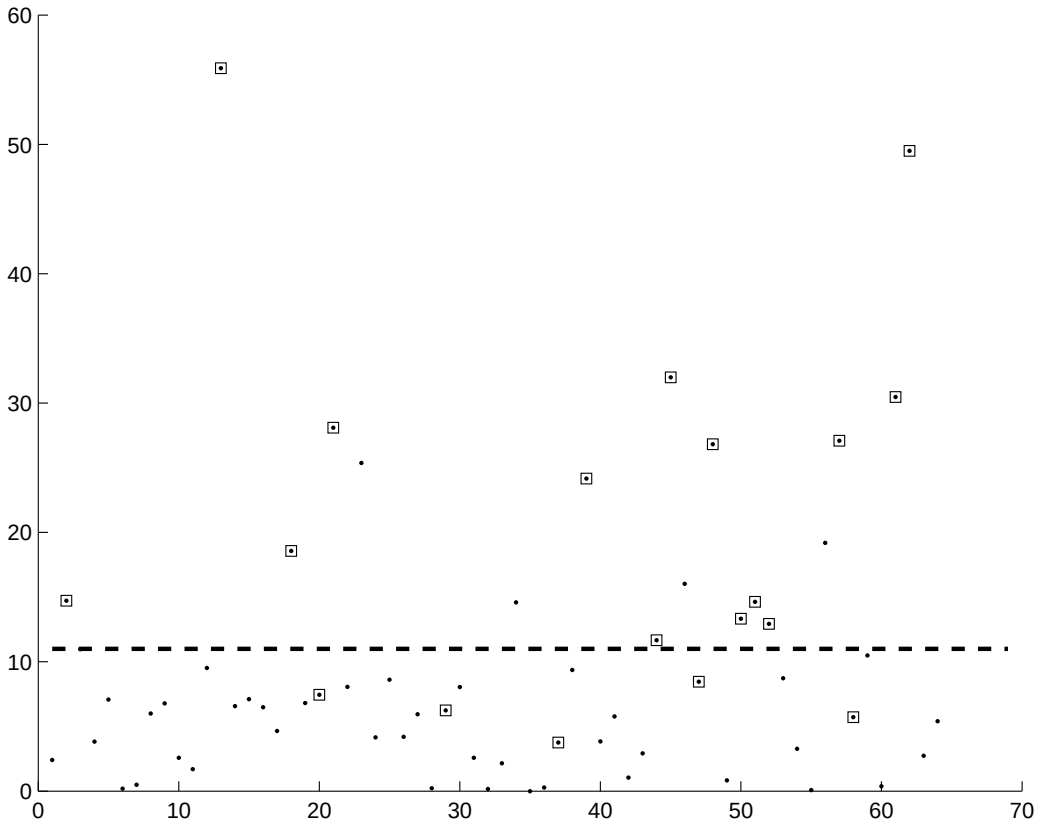

Figure 5.3: Difference between left and right neck-shaft angles. The dotted line denotes the classification threshold.

5.1.2 Test Results

	Left Femur	Right Femur	Left & Right	Difference
Correct Classification				
as fracture	12	3	15	14
as healthy	49	57	106	41
sub-total	61 (95.3%)	60 (93.8%)	121 (94.5%)	55 (85.9%)
Wrong classification				
as fracture	2	1	3	4
as healthy	1	3	4	5
sub-total	3 (4.7%)	4 (6.2%)	7 (5.5%)	9 (14.1%)
Total	64	64	128	64

Table 5.1: Summary of classification results.

ond column contains the result for the left femur, the third column contains the result for the right femur and the fourth column contains the combined results for the left and right femur. The fifth column shows the results using the neck-shaft angle difference.

Using a neck-shaft angle thresholding classifier, we can achieve an accuracy of 95.3% and 93.8% for the left and right femurs respectively. The overall accuracy for all the femurs is 94.5%. Misclassification rate is 4.7% for the left femur and 6.2% for the right femur. The combined misclassification rate is 5.5%. Out of 19 fractured cases, the classifier manages to detect 15 correctly (i.e, 80% of the total number of fractured femurs) and 4 are are wrongly classified as healthy.

Using the neck-shaft angle difference between the left and right femurs to classify the radiographic images, 55 images were correctly classified and accuracy for correct classification is 85.9%. For the misclassifications, out of 55 images, 4 images were wrongly classified.

5.1.3 Discussion on Classification Results

The algorithm has performed very well in classifying individual femurs based on neck-shaft angle. For example, for the femurs in Figure 5.4, the neck shaft angles were correctly measured and correctly classified as healthy. The

5.1.3 Discussion on Classification Results

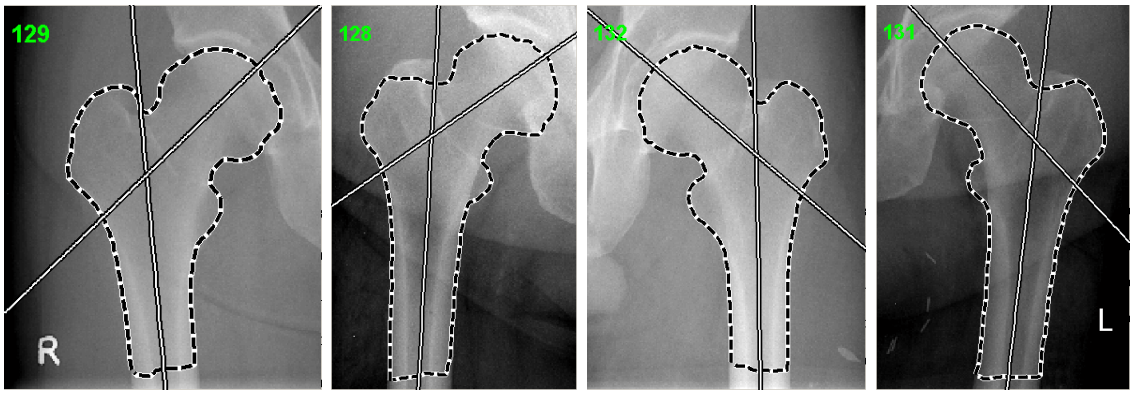

(a) (b) (c) (d)

Figure 5.4: Femurs correctly classified as healthy .

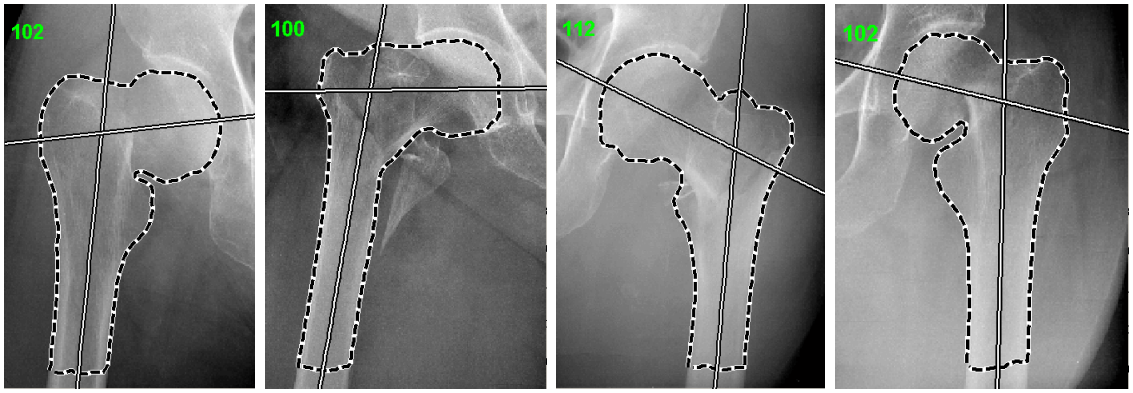

(a) (b) (c) (d)

Figure 5.5: Femurs correctly classified as fractured.

5.1.3 Discussion on Classification Results

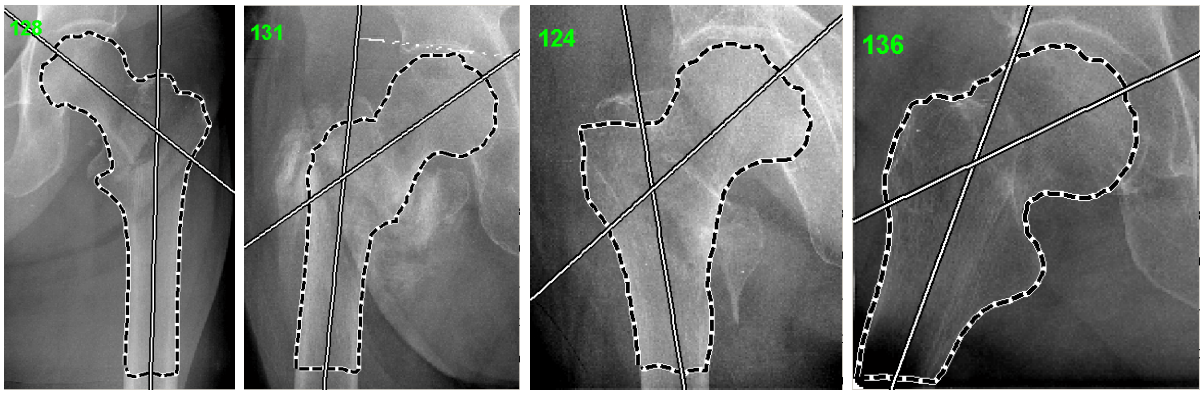

(a) (b) (c) (d)

Figure 5.6: Fractured femurs in (a) and (b) are wrongly classified as healthy due to small change in neck-shaft angle. Fractured femurs in (c) and (d) are wrongly classified as there is no change in neck-shaft angle.

femurs in Figure 5.5 were correctly classified as fractured and the neck-shaft angles were also correctly measured. There are two main reasons for the misclassification of fractured femurs as healthy femurs. The first reason is due to the fact that the fractures are not severe enough to change the neck-shaft angle significantly. For example in Figure 5.6(a) and (b) both femurs are fractured at the intertrochanteric region but the change in neck-shaft angle is not significant enough to be detected by the classified. For the second type of misclassification, a fracture has occurred but there is no change in neck-shaft angle of the femur. For example, in Figure 5.6(c) and (d). Such

5.1.3 Discussion on Classification Results

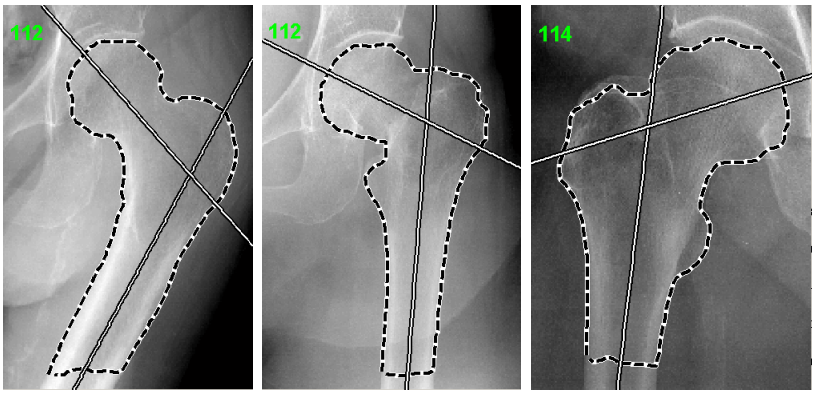

(a) (b) (c)

Figure 5.7: The x-rays of (a),(b) and (c) were not taken in the expected posture hence causing the classifier to fail.

fractures usually occur when the fracture occurs in the femoral neck region and the femoral neck is shortened but the neck-shaft angle is unchanged.

The main reason for misclassification of healthy femurs as fractured is due to the fact that the femurs were not taken in the expected position hence distorting the measured neck-shaft angle (Figure 5.7).

For the misclassification using left-right neck-shaft angle difference, the errors are similar to those encountered when classifying individual femur bone. Femur bones that are not taken in the expected position will distort the measured neck-shaft angle and the difference between the two femurs will be inaccurate hence flagging off a false alert.

Chapter 6

Future Work

In summary, the two main reasons for misclassification are:

1. Insufficient deformation in the shape to cause a large change in the neck-shaft angle

2. Fractured femurs with no change in neck-shaft angle.

To solve problem (1) it is suggested that other ways of detecting fractures be tried. For example, another feature to extract for diagnosing femur fractures is the texture of trabecular lines (Figure 6.1). Such lines run from the shaft of the femur through the neck and ending near the head of the femur. A fracture in the neck of the femur will usually disrupt the smooth running of these lines and an analysis of such pattern to pick up any major changes in the trabecular pattern is useful for locating the fracture site.

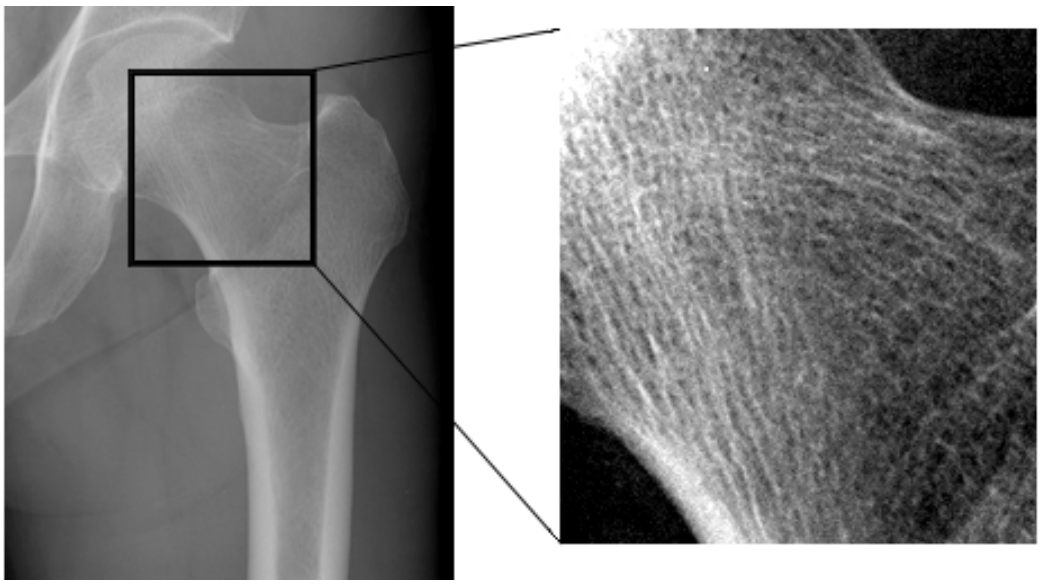

Figure 6.1: Trabecular lines.

To solve problem (2) other measurements of the femur bone have to be taken. An example will be measuring the ratio of the length of the femur neck to other parts of the femur.

With the algorithms proposed, the neck-shaft angle of a front-view x-ray image of the femur can be calculated. A more accurate method of measuring neck-shaft angle can be computed using two x-ray images. The second x-ray is taken at an oblique angle to the first. This approach takes into account 3D structure of the femur bone and based on the projection of the femur bone on two different planes the neck shaft angle in 3D can be computed. This method have been used in [28] to manually measure the neck-shaft angles in

young patients.

Chapter 7

Conclusion

In this thesis, we study the problem of estimating neck-shaft angle from the contour of the femur. A method is proposed to compute neck-shaft angle. The method comprises two algorithms. The first algorithm extracts the femur contour accurately from x-Ray images and the second algorithm computes neck-shaft angle based on the contour of the femur. The contributions of this research includes the following :

1. Developing two algorithms that form the core of a system to assist doctors in detecting femur fractures.

2. A computational method of measuring the neck-shaft angle which is more consistent and reproducible compared to manual measurement.

To the best of our knowledge, this is the first computer algorithm for measuring the neck-shaft angle from x-ray images and using neck-shaft angle to discriminate healthy femurs from fractured femurs. From the experiments conducted, we have shown that using the neck-shaft angle measured by our algorithm we can achieve a classification accuracy of 94.5%. In summary, this research has provided a basis for future research in femur fracture detection and developing algorithms to assist doctors in diagnosing fractures.

Bibliography

[1] A. Amini, T. Weymouth, and R. Jain. Using dynamic programming for solving variational problems in vision. *IEEE Transaction on Pattern Analysis and Machine Intelligence*, 12(9):855–867, 1990.

[2] Y. Amit. Graphical shape templates for automatic anatomy detection with applications to MRI brain scans. *IEEE Transactions on Medical Imaging*, 16(1), February 1997.

[3] Y. Amit and A. Kong. Graphical template for model registration. *IEEE Transaction on Pattern Analysis and Machine Intelligence*, 18(3), March 1996.

[4] H. Asada and M. Brady. The curvature primal sketch. *IEEE Transactions on Pattern Analysis and Machine Intelligence*, 8(1):2–14, January 1986.

[5] G. Behiels, F. Maes, D. Vandermeulen, and P. Suetens. Evaluation of image features and search strategies for segmentation of bone structures in radiographs using active shape models. *Medical Image Analysis*, 6(1):47–62, March 2002.

[6] F. L. Bookstein. Landmark methods for forms without landmarks : Morphometrics of group differences in outline shape. *Medical Image Analysis*, 1(3):225–243, 1997.

[7] J. Canny. A computational approach to edge detection. *IEEE Transactions on Pattern Analysis and Machinie Intelligence*, 8(6):679–698, 1986.

[8] C. C. Change, S. M. Hwang, and D. J. Buehrer. A shape recognition scheme based on relative distances of feature points from the centroid. *Pattern Recognition*, 1991.

[9] L. D. Cohen. Note on active contour models and ballons. *CVGIP : Image Understanding*, 53(2):211–218, March 1991.

[10] L. D. Cohen and I. Cohen. Finite-element methods for active contour models and ballons for 2-D and 3-D images. *IEEE Transaction on Pattern Analysis and Machine Intelligence*, 15(11):1131–1147, 1993.

[11] T. Cootes and C. J. Taylor. Statistical models of appearance for computer vision. Draft report, available at http://www.wiau.man.ac.uk, 1999.

[12] T. F. Cootes, A. Hill, C. J. Taylor, and J. Haslam. Use of active shape models for locating structres in medical images. *Image Vision Computing*, 12:355–365, 1994.

[13] T. F. Cootes, C. J. Taylor, and D. H. Cooper. Active shape models - their training and application. *Computer Vision and Image Understanding*, 61(1), January 1995.

[14] T. F. Cootes, C. J. Taylor, D. H. Cooper, and J. Graham. Training models of shape from sets of examples. In *Proc. of British Machine Vision Conference*, pages 9–18. Springer-Verlag, 1992.

[15] I. L. Dryden and K. V. Mardia. *Statistical Shape Analysis*. John Wiley & Sons, 1998.

[16] P. J. Evans and B. J. McGrory. Fractures of the proximal femur. *Hospital Physician*, April 2002.

[17] P. Golland and W. E. L. Grimson. Fixed topology skeletons. In *Proc. of IEEE Computer Vision and Pattern Recognition*, pages 10–17, 2000.

[18] C. Goodall. Procrustes methods in the statistical analysis of shape. *Journal of the Royal Statistical Society B*, 53:285–339, 1991.

[19] J. S. Gregory, D. Testi, R. E. Undrill, and R. M. Aspden. Hip fractures, morphometry and geometry. In *Proc. of 29th European Symposium on Calcified Tissues*, 2002.

[20] L. Gupta, M. R. Sayeh, and R. Tammana. A neural network approach to robust shape classification. *Pattern Recognition*, 1990.

[21] S. Haykin. *Neural Networks: A Comprehensive Foundation*. Prentice-Hall, 2nd edition, 1991.

[22] I. T. Jolliffee. *Principal Component Analysis*. Springer Verlag, 1996.

[23] M. Kass, A. Witkin, and D. Terzopoulos. Snakes: Active contour models. *International Journal of Computer Vision*, 1:321–331, 1988.

[24] W. K. Leow and R. Li. Adaptive binning and dissimilarity measure for image retrieval and classification. In *Proc. of IEEE Computer Vision and Pattern Recognition*, 2001.

[25] K. V. Mardia, J. T. Kent, and A. N. Walder. Statistical shape models in image analysis. In E Keramidas, editor, *Proc. of Computer Science and Statistics : 23rd INTERFACE Symposium*, pages 550–557, 1991.

[26] F. Mokhtarian and A. Mackworth. Scale-based description and recognition of planar curves and two dimensional shapes. *IEEE Transactions on Pattern Analysis and Machine Intelligence*, 8(1):34–43, January 1986.

[27] F. Mokhtarian and H. Muraase. Silhouette-base object recognition through curvature scale space. In *Proc. of International Conference on Computer Vision*, pages 269–274, 1993.

[28] K. Ogata and E. M. Goldsand. A simple biplanar method of measuring femoral anteversion and neck shaft angle. *The Journal of Bone and Joint Surgery*, 61-A(6):846–851, 1979.

[29] S. M. Pizer, D. H. Eberly, B. S. Morse, and D. S. Fritsch. Zoom invariant vision of figural shape: The mathematics of cores. *Computer Vision Image Understanding*, 69:55–71, 1998.

[30] S. M. Pizer, D. Fritsch, P. A. Yushkevich, V. E. Johnson, and E. L. Chaney. Segmentation, registration and measurement of shape variation via image object shape. *IEEE Transactions on Medical Imaging*, 18, Oct 1999.

[31] D. Terzopolous, J. Platt, A. Barr, and K. Fleischer. Elastically deformable models. *Computer Graphics*, 21(4):205–214, 1987.

[32] D. Terzopolous, A. Witkin, and M. Kass. Constraints on deformable models : recovering 3D shape and nonrigid motion. *Artificial Intelligence*, 36:91–123, 1988.

[33] M. K. Wong, Arjandas, L. K. Ching, S. L. Lim, and N. N. Lo. Osteoporotic hip fractures in Singapore - costs and patient's outcome. *Ann Acad Med Singapore*, 2002.

[34] C. Xu and J. L. Prince. Gradient vector flow : A new external force for snakes. In *Proc. of IEEE Conference on Computer Vision and Pattern Recognition*, 1997.

[35] C. Xu and J. L. Prince. Snakes,shapes, and gradient vector flow. *IEEE Transactions on Image Processing*, 1997.

[36] A. L. Yuille, P. W. Hallinan, and D. S. Cohen. Feature extraction from faces using deformable templates. *International Journal of Computer Vision*, 8:99–111, 1992.